https://doi.org/10.5194/egusphere-2026-6748
Preprint. Discussion started: 19 November 2026
© Author(s) 2026. CC BY 4.0 License.

Observation-constrained black carbon size and mixing state improve global simulations of aerosol optical properties

Nuo Chen[1], Ganzhen Chen[1], Weihua Ai[1,*]

1. College of Meteorology and Oceanography, National University of Defense Technology, Changsha, 410073, China

Correspondence: Weihua Ai (aiweihua@nudt.edu.cn)

Abstract

Black carbon (BC) is among the strongest warming aerosols and exerts substantial climatic impacts, yet global atmospheric models employ oversimplified representations of BC mixing state and microphysical properties, which introduce substantial biases and uncertainties in simulated BC optical properties. Here we build an explicit chain from process-level optical simulations to observation-constrained model scheme development. Particle-resolved optical sensitivity experiments spanning wavelength, refractive index, core size, coating thickness rank the sensitivity of the BC mass absorption coefficient (MAC) to each microphysical attribute. The particle-to-BC diameter ratio (D_p/D_{BC}) is identified as the dominant controllable attribute that a model can diagnose and that observations can constrain, and therefore as the natural lever for scheme improvement. Accordingly, two observation-constrained optical schemes are implemented in the Community Atmosphere Model version 6. The D_{BC}-constrained scheme applies constraints on the volume-equivalent diameters of freshly emitted BC from fossil-fuel and biomass-burning sources. This adjustment reduces the global mean D_p/D_{BC} from 6.3 to 2.1, consistent with field observations. Validated against AERONET retrievals, this scheme lowers the global normalized mean bias (NMB) of the single-scattering coalbedo from 36% to −3%, with regional reductions of 16%~70% over the BC source regions. The f_{BC}-constrained scheme incorporates regionally observed number fractions of BC-containing particles and reduces NMB of simulated MAC by

https://doi.org/10.5194/egusphere-2026-6748
Preprint. Discussion started: 19 November 2026
© Author(s) 2026. CC BY 4.0 License.

13%~68% over the representative regions. The two schemes offer a practical, observation-anchored route to more accurate BC optics and less uncertain assessments of aerosol absorption.

1. Introduction

Black carbon (BC) aerosol, the strongly absorbing particle in the atmosphere, exerts profound impacts on the climate system. Bond et al. (2013) estimated that the direct radiative forcing of BC is 0.71 (0.08 to 1.27) $W \cdot m^{-2}$, making it the second most important anthropogenic warming agent. The Intergovernmental Panel on Climate Change (IPCC) Sixth Assessment Report (AR6) expanded the assessment framework to effective radiative forcing (ERF) and revised the BC ERF estimate downward to 0.17 (−0.19 to 0.40) $W \cdot m^{-2}$. However, it emphasized that significant uncertainties persist in the radiative effects of BC aerosol, with biases in the simulation of BC optical properties being a primary source (Szopa et al., 2021; Everett et al., 2022).

Oversimplified assumptions of BC mixing state are one of the main reasons for the significant deviations in the simulations of current models. (Curci et al., 2019; Chen et al., 2023). BC is emitted into the atmosphere through the incomplete combustion of fossil fuels (FF) and biomass burning (BB). It experiences atmospheric aging and becomes coated with non-absorbing components, which produces the “lens effect” that enhances light absorption. Field observations show that the absorption enhancement (E_{abs}) is generally below 1.5 (Cappa et al., 2012; Fierce et al., 2015, 2020). Global climate models primarily describe the mixing state of BC using three idealized configurations namely external mixing (EM), volume mixing (VM), and the core-shell (CS) model. The EM model treats BC and its coating as independent particles, neglecting the “lens effect” and thereby underestimating the absorptive capacity of aged BC. Internal mixing models, including VM and CS models, ignore the heterogeneous size distribution and mass distribution of particle populations, leading to generally overestimated model predictions of E_{abs} , typically ranging from 1.5 to 2 (Curci et al., 2019; Chen et al., 2023; Fierce et al., 2020; Jacobson, 2001; Wang et al., 2021). Chen et al. (2024) found that simply optimizing the characterization of the mixing state resulted in a change of ~20% in the global average absorbent aerosol optical depth (AAOD), further confirming that the mixing-state assumption is a major source of bias in optical simulations.

In global atmospheric models, representations of BC mixing state are jointly

https://doi.org/10.5194/egusphere-2026-6748
Preprint. Discussion started: 19 November 2026
© Author(s) 2026. CC BY 4.0 License.

determined by the size and number of the BC particles. Observations from the Single-Particle Photometer (SP2) indicate that the particle-to-BC-core diameter ratio (D_p/D_{BC}), which is widely adopted to quantify the extent of BC mixing, is concentrated within a narrow range of 1.2~3.5 (Shiraiwa et al., 2007; Ditas et al., 2018; Zanatta et al., 2018). Since the mass absorption coefficient (MAC) exhibits a strong nonlinear dependence on the ratio D_p/D_{BC}, such microphysical uncertainties are amplified into substantial optical biases (Romshoo et al., 2021; Wang et al., 2021). In contrast, current models assume that BC is uniformly distributed across all particles within a given mode/bin, which often leads to abnormally high D_p/D_{BC} and thus introduces systematic biases in optical calculations (Chen et al., 2023; Fierce et al., 2020; Schwarz et al., 2008). The uniform BC mass-allocation assumption also implies that the fraction of BC-containing particles (f_{BC}) is 100%, inconsistent with aerosol mixing states in real atmosphere. Observations show that f_{BC} varies significantly across different locations. In urban polluted air, it can reach 60%~80%, whereas it drops to a few percent in remote background areas (Chen et al., 2020; Cheung et al., 2016; Ma et al., 2020; Kodros et al., 2018; Schwarz et al., 2006). Kodros et al. (2018) further incorporated observation-constrained f_{BC} into GEOS-Chem simulations and found that it reduced the uncertainty in the direct radiative effect in the Arctic by a factor of 2, confirming that the incorporation of observation constraints has a significant impact on optical simulation results. In summary, improving the model's characterization of BC mixing states and physicochemical properties is a key optimization direction for reducing uncertainties in BC optical simulations.

In this study, we quantified the response of BC optical properties to microphysical parameters through particle-resolved sensitivity experiments and identified the most sensitive and observation-constrained external parameters. According to these findings, we develop two observation-constrained schemes namely D_{BC}-constrained scheme and f_{BC}-constrained scheme based on Community Atmosphere Model version 6 (CAM6). Sect. 2 describes the setup of sensitivity experiments, model configurations of the two schemes, and descriptions of observation data. Sect. 3.1 presents the results of sensitivity tests. Sect. 3.2~3.3 illustrate the improvements in optical simulations relative to observations for the new schemes, respectively, and evaluate the stability of the schemes at the microphysical level.

https://doi.org/10.5194/egusphere-2026-6748
Preprint. Discussion started: 19 November 2026
© Author(s) 2026. CC BY 4.0 License.

2. Methods

2.1 Optical calculations for aerosol mixing states

In the EM state, BC and the coating material exist as separate particles that retain their individual refractive indices. Optical signals from BC and non-BC components are computed separately and then combined linearly. The VM state instead homogeneously blends BC with the coating material within a single particle, whose effective complex refractive index m_{eff} is obtained by volume-weighted averaging:

$$m_{eff}=\frac{V_{BC}\cdot m_{BC}+\sum_i V_i\cdot m_i}{V_{total}} \quad (1)$$

where V_{BC} and m_{BC} denote the volume and complex refractive index of BC, and V_i and m_i those of the non-BC component. Because the strongly absorbing refractive index of BC is diluted within m_{eff}, the intrinsic absorption of BC is systematically weakened when its volume fraction is low.

The CS state provides a more physically realistic representation, in which BC forms a compact core of diameter D_{BC} fully encapsulated by a non-absorbing shell of total diameter D_p. The optical properties are computed by the core-shell Lorentz-Mie theory (Toon and Ackerman, 1981). In contrast to VM, the CS state preserves the pure refractive index of the BC core, so that the shell enhances absorption solely through the lensing effect. Sensitivity experiments are then conducted within these three mixing-state frameworks to quantify their distinct optical responses and to identify the key parameters governing BC optical properties.

The Mie algorithm outputs the extinction, absorption, and scattering efficiency factors (Q_{ext},Q_{abs},Q_{sca}), together with the asymmetry parameter (ASY). Calculations are performed for homogeneous-sphere representations under the EM and VM assumptions, as well as for CS geometries following Toon and Ackerman (1981). All calculations are constrained to the physically meaningful domain satisfying $D_p \geq D_{BC}$. Corresponding particle cross-sections are obtained as the product of each efficiency factor and the particle geometric cross-section:

$$C_{ext/abs/sca}=Q_{ext/abs/sca}\cdot\frac{\pi D_p^2}{4} \quad (2)$$

For single-particle sensitivity analyses, cross-sections are normalized by BC core mass:

https://doi.org/10.5194/egusphere-2026-6748
Preprint. Discussion started: 19 November 2026
© Author(s) 2026. CC BY 4.0 License.

$$M_{BC}=\pi\rho_{BC}D_{BC}^3/6 \quad (3)$$

where the density of black carbon is $\rho_{BC}=1700\ kg\ m^{-3}$ (Zhao et al., 2021). This normalization yields the mass-resolved optical coefficients MAC, mass-extinction coefficient (MEC), and mass-scattering coefficient (MSC):

$$MAC/MEC/MSC=\frac{3\ Q_{abs/ext/sca}\ D_p^2}{2\ \rho_{BC}\ D_{BC}^3} \quad (4)$$

The single-scattering albedo (SSA) describes the scattering fraction of total particle extinction, and 1−SSA denotes the fractional contribution of absorption:

$$SSA=\frac{Q_{sca}}{Q_{ext}}=1-\frac{MAC}{MEC} \quad (5)$$

The asymmetry parameter (ASY) quantifies the forward-to-backward anisotropy of the scattering phase function:

$$ASY=g=\frac{\int_0^\pi P(\theta)\cos\theta\sin\theta\ d\theta}{\int_0^\pi P(\theta)\sin\theta\ d\theta} \quad (6)$$

All five optical quantities are evaluated for EM, VM, and CS states across varying D_{BC}, D_p, wavelength, and complex refractive-index conditions.

2.2 Sensitivity Quantification Methods

To quantify the relative contributions of microphysical parameters and their interactions to the variance of MAC, a global sensitivity analysis based on Sobol variance decomposition (Sobol, 2001) is applied to the offline Mie calculations, utilizing CS mixing state with MAC as the model output variable Y. The method decomposes the total variance V of the output into fractions attributable to each input parameter and to their interactions. The first-order sensitivity index S_i measures the fractional contribution of parameter x_i alone:

$$S_i=\frac{V_i}{V}=\frac{Var_{x_i}\left[E_{x_{\sim i}}(Y\mid x_i)\right]}{Var(Y)}, \quad (7)$$

where Y is the model output (MAC), V_i is the variance of the conditional expectation of Y given x_i, and $x_{\sim i}$ denotes all parameters except x_i. The total-order index S_{Ti} captures the total contribution of x_i, including all of its interactions with the remaining parameters:

$$S_{Ti}=S_i+\sum_{jj\neq i}S_{ij}+\sum_{j<k,\,j,k\neq i}S_{ijk}+\cdots=\frac{E_{x_{\sim i}}\left[Var_{x_i}(Y\mid x_{\sim i})\right]}{Var(Y)}. \quad (8)$$

As summarized in Table 1, five input parameters are considered, each sampled

https://doi.org/10.5194/egusphere-2026-6748
Preprint. Discussion started: 19 November 2026
© Author(s) 2026. CC BY 4.0 License.

uniformly over its range. However, it should be noted that the input range is determined by the range of BC's microphysical parameters in the current model (Bond and Bergstrom, 2006; Liu et al., 2012, 2016). Therefore, the resulting sensitivity ranking can provide a theoretical basis for optimizing the current BC optical parameterization scheme, but cannot be regarded as a universal characteristic of the BC Mie scattering model.

The specific calculation is based on the extended design methodology proposed by Saltelli et al. (2010), which yields reduced mean-squared error at a computational cost of N(2p + 2) model evaluations for p parameters. Two independent N×p base sample matrices, A and B, are first generated. For each parameter x_i, two additional mixed matrices, $A_B^{(i)}$ and $B_A^{(i)}$, are then constructed by replacing the i-th column of A (B) with the corresponding column of B (A) while leaving all other columns unchanged. Denoting by Y_A, Y_B, Y_{AB_i}, and Y_{BA_i} the model outputs evaluated on A, B, $A_B^{(i)}$ and $B_A^{(i)}$, respectively, the indices are estimated as:

$$\hat{S}_i = \frac{\frac{1}{N}\sum_{j=1}^{N} Y_B^{(j)}\left(Y_{AB_i}^{(j)} - Y_A^{(j)}\right) + \frac{1}{N}\sum_{j=1}^{N} Y_A^{(j)}\left(Y_{BA_i}^{(j)} - Y_B^{(j)}\right)}{2V}, \quad (9)$$

$$\hat{S}_{Ti} = \frac{\frac{1}{N}\sum_{j=1}^{N}\left(Y_A^{(j)} - Y_{AB_i}^{(j)}\right)^2 + \frac{1}{N}\sum_{j=1}^{N}\left(Y_B^{(j)} - Y_{BA_i}^{(j)}\right)^2}{4V}, \quad (10)$$

where V is the total variance of the pooled outputs $\{Y_A, Y_B\}$. Bootstrap resampling (1000 replicates) is applied to obtain the 95% confidence intervals for first- order and total- order Sobol indices (Archer et al., 1997).

Table 1. Microphysical variables used in sensitivity experiments

Parameter	Symbol	Range	Baseline value
BC core diameter	D_{BC}	5~110 nm	61 nm
particle-to-BC-core diameter ratio	D_p/D_{BC}	1~20	6.3
Real part of BC refractive index	Re	1.0~2.0	1.95
Imaginary part of BC refractive index	Im	0.4~1.2	0.79

https://doi.org/10.5194/egusphere-2026-6748
Preprint. Discussion started: 19 November 2026
© Author(s) 2026. CC BY 4.0 License.

Wavelength	λ	200~1000 nm	550 nm

To complement these global and variance-based indices with local sensitivity information, the absolute normalized sensitivity coefficient |NSC| is further computed for each parameter:

$$|\mathrm{NSC}|=\left|\frac{\partial \ln \mathrm{MAC}}{\partial \ln x_i}\right| \approx \left|\frac{\Delta \mathrm{MAC}/\mathrm{MAC}}{\Delta x_i/x_i}\right| \quad (11)$$

Compared to the Sobol indices, which provide an integrated measure of parameter importance over the entire parameter space, |NSC| reveals how the local sensitivity of MAC to each parameter varies across the parameter space, particularly as a function of D_p/D_{BC}. Together, the Sobol indices identify the dominant parameter in terms of variance contribution, whereas |NSC| characterizes the regime dependence of that sensitivity. These quantitative results directly motivate the design of the observation-constrained schemes.

2.3 Description of CAM6 Model and Simulation Settings

All simulations are performed with the CAM6, which serves as the atmospheric component of the Community Earth System Model (CESM) version 2 (Danabasoglu et al., 2020). Aerosol microphysics is represented by the four-mode Modal Aerosol Module (MAM4), which categorizes aerosols into the Aitken, accumulation, coarse, and primary carbon modes (Liu et al., 2012, 2016). Each mode carries up to six species, including sulfate, secondary organic matter, sea salt, primary organic matter, BC, and dust, with mass concentrations for individual components and number concentrations for each mode. Among these, BC is confined to the accumulation and primary carbon modes. The size distribution of each mode follows a lognormal function, with geometric mean diameters spanning 0.015~0.053 μm (Aitken), 0.058–0.48 μm (accumulation), 0.4–40 μm (coarse), and 0.06~0.3 μm (primary carbon). Particles are assumed to be internally mixed within a given mode and externally mixed across modes.

For aerosol optical properties, CAM6 employs the parameterization of Ghan and Zaveri (2007), in which the volume-averaged wet refractive index and the hygroscopically grown wet radius of each mode are used to compute the mass extinction, absorption, and asymmetry factor via Mie theory. These optical outputs feed into the shortwave radiative transfer solver, the Rapid Radiative Transfer Model

https://doi.org/10.5194/egusphere-2026-6748
Preprint. Discussion started: 19 November 2026
© Author(s) 2026. CC BY 4.0 License.

for GCMs (RRTMG; Iacono et al., 2008).

The model is run at a horizontal resolution of 1.9° × 2.5° (latitude × longitude) with 32 vertical hybrid-sigma pressure levels extending from the surface to approximately 3 hPa. Monthly mean outputs spanning 2010~2020 are used for analysis. The component densities and refractive index parameters are listed in Table 2. RI values for BC are from Bond and Bergstrom (2006) and those for other components are from the OPAC database (Hess et al., 1998).

Table 2. Aerosol component densities and refractive indices (RI) at shortwave wavelengths (440~625 nm).

Species	Density (g/cm3)	RI
BC	1.7	1.95 + 0.79i
Primary organic matter	1.0	1.53 + 0.0006i
Secondary organic matter	1.0	1.53 + 0.0006i
Dust	2.6	1.56 + 0.0019i
Sulfate	1.77	1.43 + 0i
Sea salt	1.9	1.5 + 0i

2.4 Description of Optical Optimization Schemes

Given that BC mixing state is characterized by two observable quantities, the core diameter D_{BC} and the number fraction of BC-containing particles f_{BC}, which govern particle geometry and the distribution of BC across the particle population, respectively. Figure 1 illustrates the conceptual designs of the three BC optical schemes in this study. The default configuration (Figure 1a) implicitly sets f_{BC}=100% and produces relatively small BC core sizes. The two schemes developed in this study impose constraints on these two observables separately. The D_{BC}-constrained scheme (Figure 1b) modifies core geometry, where the core diameter of BC-containing particles is prescribed by source-resolved BC size distributions from observations. The f_{BC}-constrained scheme (Figure 1c) constrains the particle population allocation. With the number fraction of BC-containing particles bounded by regional observations, the same total BC mass is concentrated into fewer particles, each carrying a larger BC core.

https://doi.org/10.5194/egusphere-2026-6748
Preprint. Discussion started: 19 November 2026
© Author(s) 2026. CC BY 4.0 License.

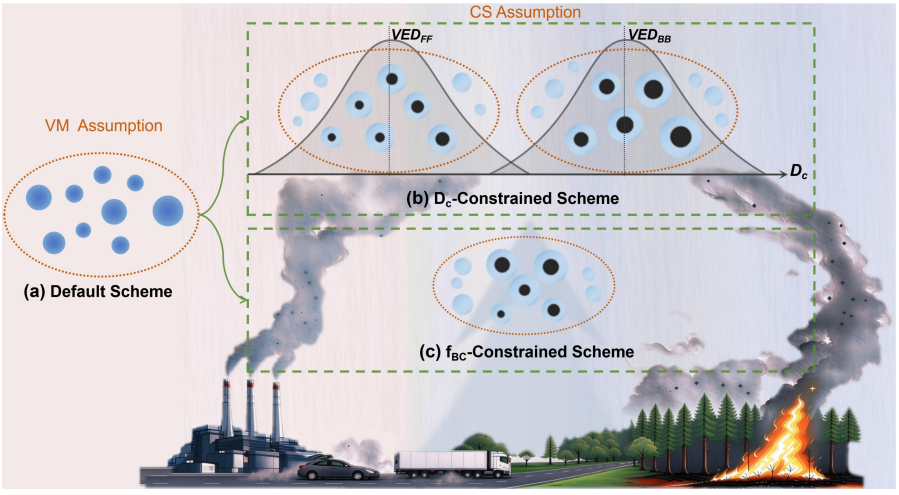


Figure 1. Schematic of the default BC optical scheme (volume mixing, VM) and the two observation-constrained schemes (core-shell model, CS): **(a)** Default scheme. All particles are assumed to carry BC uniformly with f_{BC} set to 100%; **(b)** D_{BC}-constrained scheme. The BC core diameter is constrained by the observed size distribution of freshly emitted BC. The volume-equivalent diameters (VED_{FF} and VED_{BB}) for fossil fuel combustion (FF) and biomass burning (BB) are derived from Bond et al. (2013). **(c)** f_{BC}-constrained scheme. BC mass is allocated only to particles with a proportion of f_{BC}. A value of f_{BC} = 50 % is shown for illustration, and the f_{BC} applied in the scheme comes from regional in-situ observations.

The default CAM6 optical treatment (Fig. 1a) adopts VM assumption, in which all aerosol components within a given mode are treated as an internally homogeneous mixture. Under this scheme, D_p and D_{BC} are calculated by distributing the total aerosol volume and BC volume, respectively, over the entire particle number concentration N of the mode:

$$D_p=\left(\frac{6\cdot V_{total}}{\pi\cdot N}\right)^{1/3} \tag{12}$$

$$D_{BC}=\left(\frac{6\cdot V_{BC}}{\pi\cdot N}\right)^{1/3} \tag{13}$$

The optical properties are subsequently computed using a volume-averaged effective refractive index m_{eff} for a homogeneous sphere:

$$MAC_{VM}=\frac{3\cdot Q_{abs}^{VM}(D_p, m_{eff}, \lambda)\cdot D_p^2}{2\cdot \rho_{BC}\cdot D_{BC}^3}, \tag{14}$$

https://doi.org/10.5194/egusphere-2026-6748
Preprint. Discussion started: 19 November 2026
© Author(s) 2026. CC BY 4.0 License.

where Q_{abs}^{VM} is the absorption efficiency factor.

The D_{BC}-constrained scheme (Fig. 1b) replaces the volume-derived core diameter with observationally constrained values. Two volume-equivalent diameters (VEDs) are obtained by fitting the size distribution statistics of freshly emitted BC particles from Bond et al. (2013), corresponding to FF combustion and BB emissions. The primary carbon mode hosts freshly emitted BC with small cores and particle sizes, and is therefore assigned VED_{FF}, whose magnitude remains within the particle size range of this mode. The accumulation mode comprises aged BC and is assigned the larger VED_{BB}. This assignment also guarantees geometric rationality ($D_{BC} < D_p$) within each mode and the supporting size-distribution evidence is presented in Section 3.2.

The f_{BC}-constrained scheme (Fig. 1c) is constrained by in-situ observational data for the number fraction of BC-containing particles. The BC mass assigned to individual BC-containing particles increases, which enlarges the core diameter D_{BC} and partially mitigates the underestimation of D_{BC} in the default configuration. Since BC exists in different aerosol modes, the total MAC value is derived via BC-mass-weighted aggregation:

$$MAC_{total} = \frac{\sum_i MAC_i \cdot M_{BC}^i}{\sum_i M_{BC}^i}. \quad (15)$$

2.5 Observation Data and Assessment Methods

The global-scale evaluation in this study uses Level 2.0 inversion products of AERONET monthly data from 2010 to 2020, which provides column-integrated, quality-assured retrievals of aerosol optical properties at wavelengths of 440, 675, 870, and 1020 nm (Dubovik & King, 2000; Holben et al., 1998). Due to that AERONET provides column-integrated retrievals, SSA is calculated by performing layer-by-layer integration on the model:

$$\overline{SSA} = \frac{\tau_{sca}}{AOD} = \frac{\sum_{l=1}^{L} \beta_{sca,l} \cdot \Delta z_l}{\sum_{l=1}^{L} \beta_{ext,l} \cdot \Delta z_l}, \quad (16)$$

where $\beta_{sca,l}$ and $\beta_{ext,l}$ are the volume scattering and extinction coefficients of layer l, Δz_l is the geometric thickness of layer l(m), and L is the number of vertical levels. The normalized mean bias (NMB) and root-mean-square error (RMSE) are used to quantify overall model–observation discrepancies.

https://doi.org/10.5194/egusphere-2026-6748
Preprint. Discussion started: 19 November 2026
© Author(s) 2026. CC BY 4.0 License.

The regional-scale evaluation of the f_{BC}-constrained scheme uses in-situ MAC measurements from six representative regions (Table 3). The observed f_{BC} and MAC values at these monitoring stations exhibit diversity, reflecting the differences among these six regions in terms of emission source types, particulate matter aging degree, and coating thickness. It should be noted that for the Chengdu site, the observed f_{BC} values are derived from field measurements at Mount Emei (Yuan et al., 2023), while the corresponding MAC values are from an urban site in Chengdu (Tao et al., 2018). For Guangzhou and the African region, the observed MAC values were not obtained directly from field measurements but were derived based on the absorption enhancement factors (E_{abs}) reported in the references (Fu et al., 2021; Brown et al., 2021; Bond and Bergstrom, 2006).

Table 3. In-situ observations of BC-related microphysical and optical properties from other studies

Region	Coordinates	f_{BC} (%)	Observed MAC (m^2/g)	Wavelength (nm)	Reference
Beijing	115°~117° E 39°~41° N	51-64	9.5±2.49	550	Chen et al. (2020); Yang et al. (2009)
Nanjing	118°~120° E 31°~33° N	62.4±27.9	11.8±3.7	532	Ma et al. (2020)
Africa	0~35° E 12° S~12° N	40	12.0±3.0	550	Holanda et al. (2020); Brown et al. (2021)
Guangzhou	112°~114°E 22°~24°N	24	8.5±1.6	520	Li et al. (2023); Fu et al. (2021)
Chengdu	104.03°E 30.65°N	54	6.5±0.4	880	Yuan et al. (2023); Tao et al. (2018)
Ascension	14.36°W 7.95° S	21-29	15.6±2.3	529	Dobracki et al. (2025); Zuidema et al. (2018)

https://doi.org/10.5194/egusphere-2026-6748
Preprint. Discussion started: 19 November 2026
© Author(s) 2026. CC BY 4.0 License.

3. Results

3.1 Sensitivity and Relative Contributions of Key Microphysical Parameters to BC Optical Properties

Our simulations reveal a strong and size-dependent sensitivity of BC optical properties to the mixing states (Figures 2 and 3). Figure 2 presents size-dependent optical properties (MAC, SSA, and ASY) of BC under EM, VM, and CS mixing states, and Figure 3 shows their relative differences. All simulations adopt a wavelength of 550 nm with prescribed BC refractive index and shell refractive index RI_{shell} = 1.55 + 0i. Both the diameter D_{BC} and D_p span 0~500 nm. For MAC, the EM state exhibits the smallest value overall; followed by the CS and the VM states. This finding is consistent with the conclusions drawn by Denjean et al. (2020) and Taylor et al. (2020). This ordering fundamentally stems from the different approaches to handling the refractive index of black carbon. The VM state assumes that the black carbon refractive index is averaged over the entire volume including the non-absorbing shell. This configuration maximizes the effective interaction cross-section between incident photons and BC, resulting in a systematic overestimation that is notably pronounced within specific size ranges. Conversely, the CS state preserves the strong absorption characteristics of the BC core, with enhancement driven solely by the ‘lens effect' of the shell layer, representing a more physically reasonable mechanism.

Notably, the mixing-state effect exhibits a pronounced size dependence. MAC typically peaks within the 100-300 nm size range (Figure 2a-c), which corresponds to the typical atmospheric aerosol regime. At larger ratio D_p/D_{BC}, the difference between the external and internal mixing states becomes most pronounced (Fig. 3a-3b). However, in this case, VM can actually simulate a lower MAC than CS. This suggests that when BC is extensively coated, the volume averaging method may overly dilute the absorption characteristics of BC (Fig. 3c).

Regarding SSA, values decrease with increasing BC core diameter D_{BC}. The transition from external to internal mixing reduces SSA for larger particles (300-500 nm), indicating that the fraction of light absorption to extinction increases as particles age. The SSA value simulated by VM is typically higher than that of CS (Fig. 3d-f). However, in cases involving small particles and thin coatings, the SSA value for VM may be lower than that for CS (Fig. 3f). This could be due to the weaker ‘lens effect'

https://doi.org/10.5194/egusphere-2026-6748
Preprint. Discussion started: 19 November 2026
© Author(s) 2026. CC BY 4.0 License.

and lower absorption efficiency associated with CS, which results in a higher SSA value compared to VM. For the asymmetry parameter (ASY), which quantifies forward scattering, values increase with total particle size (D_p). Both VM and CS mixed particles exhibit stronger forward scattering than EM particles across the entire size range, with VM generally yielding a higher ASY than CS (Fig. 3g-i).

Overall, these results confirm that the optical characterization of BC in atmospheric models must carefully account for both the mixing-state hypothesis and the particle size ranges to avoid substantial biases in radiative transfer calculations. These size-dependent effects, particularly the non-monotonic variations in MAC and SSA observed across different coating thicknesses, underscore the critical importance of both mixing state and D_p/D_{BC} for BC optical properties.

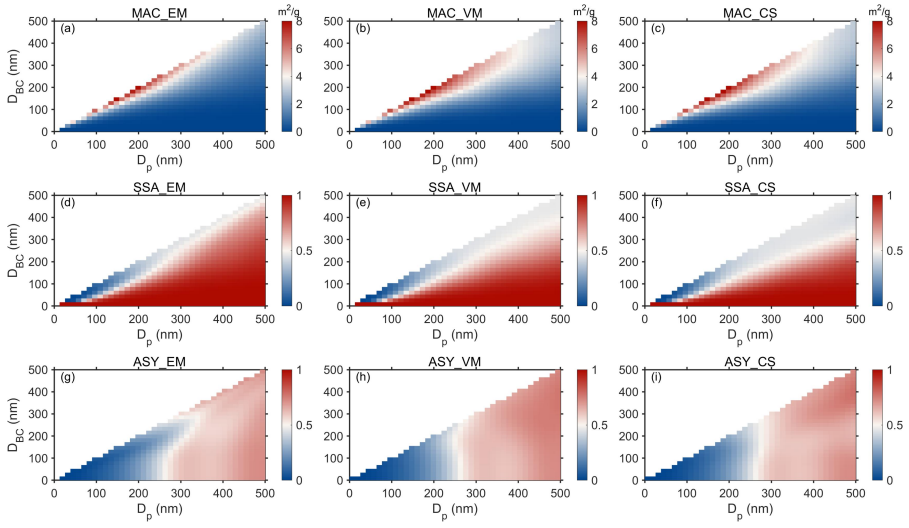


Figure 2. Optical properties of BC under different mixing states as a function of total particle size (D_p) and BC core diameter (D_{BC}): **(a-c)** Mass absorption coefficient (MAC, m²/g) for external mixing (EM), volume internal mixing (VM), and core-shell mixing (CS), respectively; **(d-f)** single-scattering albedo (SSA); **(g-i)** asymmetry parameter (ASY) at λ=550nm.

https://doi.org/10.5194/egusphere-2026-6748
Preprint. Discussion started: 19 November 2026
© Author(s) 2026. CC BY 4.0 License.

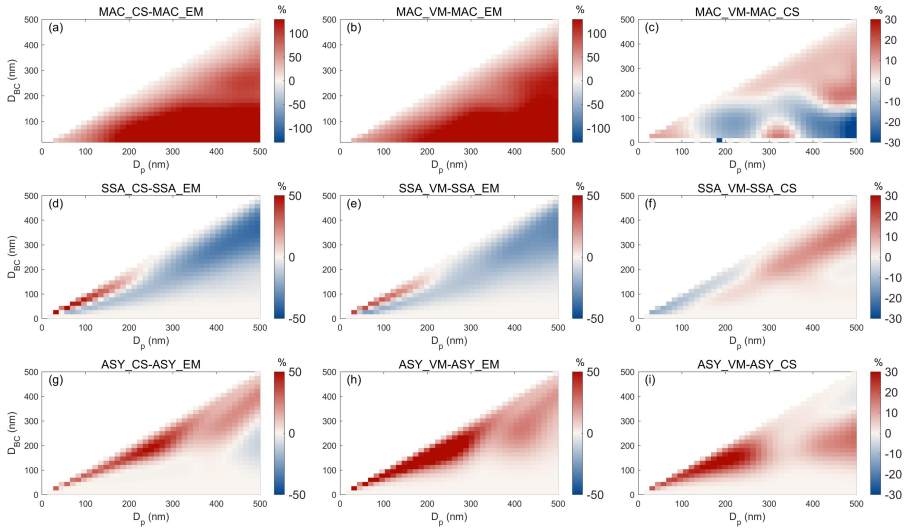


Figure 3. Relative differences in optical properties among mixing states of BC: **(a-c)** Relative differences in MAC between CS vs. EM, VM vs. EM, and VM vs. CS, respectively; **(d-f)** SSA; **(g-i)** ASY at λ=550nm.

Having established the strong sensitivity of BC optical properties to mixing state and coating thickness, we extend our sensitivity analysis to two additional controls, namely the incident wavelength and the complex refractive index of BC. The wavelength governs the absorption-scattering balance through the size parameter ($x = \pi D/\lambda$), while the complex refractive index determines the intrinsic absorption capacity of BC. Figure 4 illustrates how the optical properties of BC (MAC and MEC) vary with wavelength under different mixing conditions. The shaded regions characterize the refractive index sensitivity across wavelengths, with the real and imaginary components of the refractive index ranging between 1.0~2.0 and 0.4~1.2, respectively. Additionally, we examine whether wavelength sensitivity differs across different D_p/D_{BC}, with the BC particle diameter fixed at 107 nm.

https://doi.org/10.5194/egusphere-2026-6748
Preprint. Discussion started: 19 November 2026
© Author(s) 2026. CC BY 4.0 License.

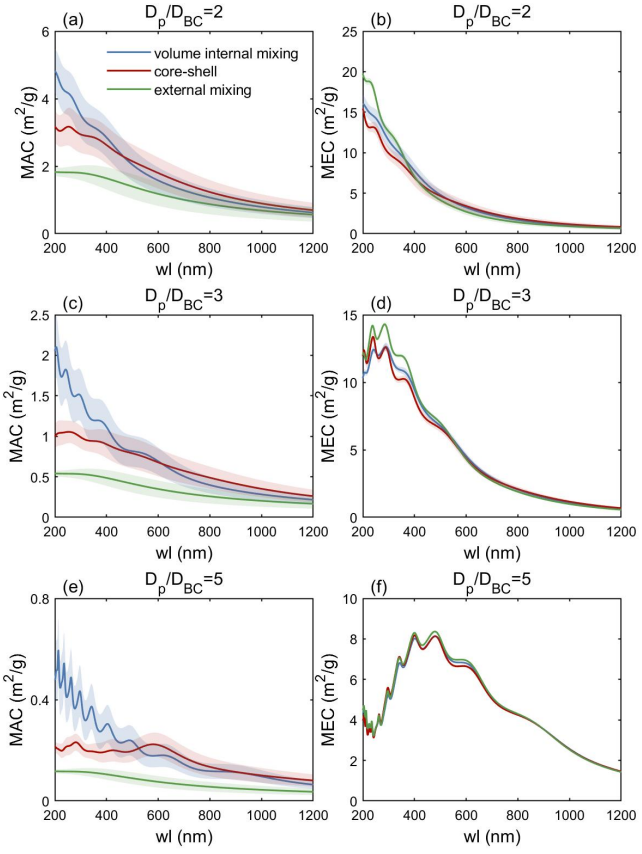


Figure 4. Variations in the optical properties of BC as a function of wavelength (wl) and the particle-to-BC core size ratio (D_p/D_{BC}) for different mixing states and refractive indices. **(a-b)** MAC and mass extinction coefficient (MEC) for D_p/D_{BC}=2; **(c-d)** D_p/D_{BC}=3;**(e-f)** D_p/D_{BC}=5. The shaded regions in each plot represent fluctuations caused by changes in the real and imaginary parts of BC's refractive index.

As can be seen from Figure 4a, c, and e, MAC decreases with increasing wavelength (200~1200 nm) across all mixing states, consistent with BC's stronger intrinsic spectral absorption behavior at short wavelengths. EM consistently yields the lowest MAC. In the short-wavelength regime (<500 nm), VM exhibits the highest MAC and the steepest decay rate, at which point its spectral sensitivity is maximized. Between 500~600 nm, MAC values for VM and CS converge, indicating reduced sensitivity to mixing state in this spectral range. At longer wavelengths (>600 nm),

https://doi.org/10.5194/egusphere-2026-6748
Preprint. Discussion started: 19 November 2026
© Author(s) 2026. CC BY 4.0 License.

differences in MAC among mixing states diminish further and absorption efficiency plateaus. At this stage, sensitivity to both the mixing states and wavelength is relatively low.

MEC exhibits a non-monotonic trend as the wavelength changes. Its value initially increases and then decreases in the short-wavelength band, which is particularly pronounced when the coating is thick (Fig. 4f). Furthermore, unlike MAC, the value of the external mixing state reaches its maximum in the short-wavelength band. As the D_p/D_{BC} value increases, both MAC and MEC decline, and the relative reduction of MEC is less pronounced as indicated by axis scales. This reflects its lower sensitivity to D_p/D_{BC} as scattering effects partially offset the decrease in absorption. The MEC values show minimal variation under different mixing conditions, particularly at longer wavelengths or for thicker coatings, where the MEC is primarily governed by scattering effects and thus remains insensitive to the absorption changes induced by the mixing state. The shaded area indicates that the refractive index of BC has a significant impact on MAC, whereas its influence on MEC is negligible. Among these, the MAC associated with the EM state exhibits the lowest sensitivity to the refractive index. Furthermore, when the coating thickness is greater, the effect of the refractive index on absorption is diminished.

Since wavelength-dependent behavior is closely related to the complex refractive index of BC, we further investigate how the variations in the real (Re) and imaginary part (Im) of BC's refractive index modulate MAC, MEC, and MSC over a representative wavelength range. Figure 5 presents these distributions under the CS state, with BC core diameter fixed at 100 nm and total particle diameter at 200 nm. The results are shown at three representative wavelengths (440 nm, 675 nm, and 1020 nm), spanning the visible to near-infrared range.

https://doi.org/10.5194/egusphere-2026-6748
Preprint. Discussion started: 19 November 2026
© Author(s) 2026. CC BY 4.0 License.

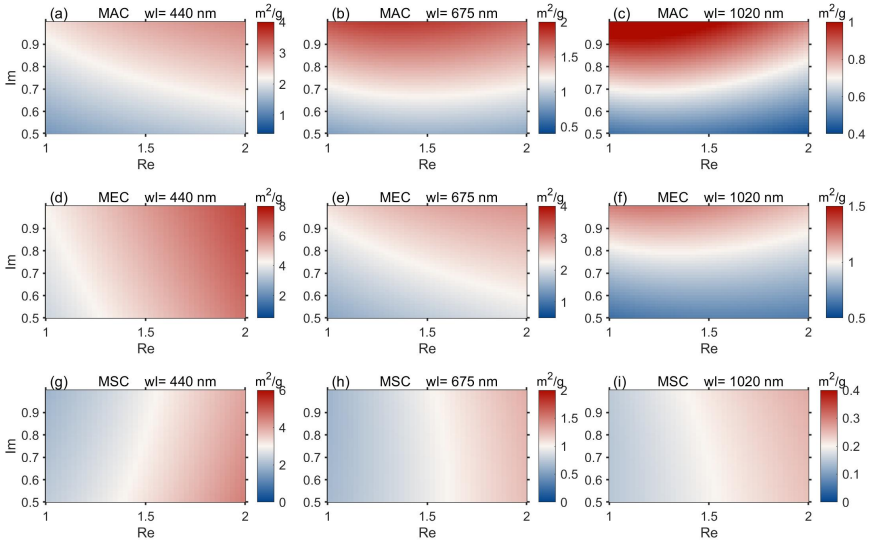


Figure 5. Distribution of optical properties of BC under the CS as functions of the real part (Re) and imaginary part (Im) of the refractive index at different wavelengths (440 nm, 675 nm, 1020 nm): **(a-c)** MAC, **(d-f)** MEC, and **(g-i)** mass scattering coefficient (MSC).

At shorter wavelengths (440 nm), MAC increases significantly with the Im of the refractive index, reaching its maximum value when Im is high, a conclusion consistent with the findings of Taylor et al. (2020). Meanwhile, MAC also increases with Re, though Re's effect is weaker than Im's. As wavelength increases to 675 nm and 1020 nm, the overall MAC value gradually decreases, and the relative increase in MAC due to Im diminishes, indicating stronger absorption capacity and greater sensitivity to Im at shorter wavelengths. Moreover, MAC's sensitivity to Re is much lower than to Im at longer wavelengths (Fig. 5b). In fact, as the Re increases, the MAC value decreases slightly (Fig. 5c).

The variation trends of MEC and MAC are quite similar , particularly in the long-wave band, where the overall value of MEC decreases and its dependence on Re diminishes (Fig. 5d–f). By comparing with the MSC (Fig. 5g-i), we find that at longer wavelengths, Im is positively correlated with both MAC and MEC, with highly consistent trends at 1020 nm. This indicates that in the long-wave region, particle extinction is primarily driven by absorption and depends mainly on Im. However, at

https://doi.org/10.5194/egusphere-2026-6748
Preprint. Discussion started: 19 November 2026
© Author(s) 2026. CC BY 4.0 License.

440 nm, MAC and MSC show opposite trends with Im, and MEC's insensitivity to Im may arise because scattering partially offsets absorption. Especially at high Re, the strong scattering effect of particles makes Im's impact on MEC negligible. These results suggest that for BC optical properties assessment in the long-wave region, Im's absorption effect can be the primary focus. In the short-wave region, absorption and scattering interact and constrain each other, necessitating simultaneous consideration of Re and Im in regulating aerosol optical properties.

Taken together, the experiments above show that MAC responds nonlinearly to both the parameter space and wavelength, with a pronounced dependence on coating thickness (D_p/D_{BC}) and wavelength. Because such one-at-a-time analyses cannot rank the contributions of individual parameters and their interactions to the overall variance of MAC, we quantify parameter importance using the complementary |NSC| and Sobol analyses.

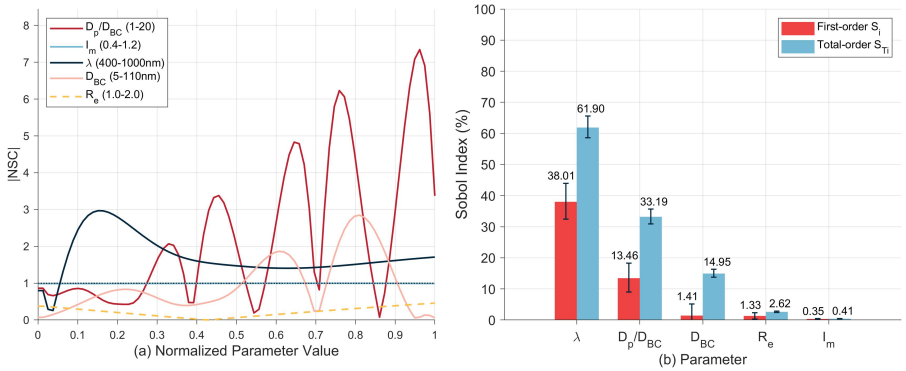


Figure 6. Normalized sensitivity coefficients (|NSC|) of BC optical properties to normalization parameters and Sobol indices of their contributions: **(a)** |NSC| as a function of normalized parameter values for particle-to-BC core size ratio (D_p/D_{BC}), imaginary part of refractive index (Im), wavelength (λ), core diameter (D_{BC}), and real part of refractive index (Re); **(b)** Sobol indices (first-order S_i and total-order S_{Ti}) quantifying the variance contributions of each parameter to MAC.

Figure 6(a) presents the absolute normalized sensitivity coefficients (|NSC|) of each parameter as functions of their normalized parameter values. The |NSC| of D_p/D_{BC} exhibits pronounced fluctuations across the entire parameter range and generally increases with increasing normalized parameter value. As the normalized value approaches unity, which means the shell thickens, |NSC| rises rapidly in an

https://doi.org/10.5194/egusphere-2026-6748
Preprint. Discussion started: 19 November 2026
© Author(s) 2026. CC BY 4.0 License.

oscillatory manner. This indicates that minute changes in shell thickness can trigger dramatic responses in MAC within this regime, which corresponds exactly to the BC size distribution adopted by the current BC optical parameterization scheme, implying that MAC is extremely sensitive to shell thickness here.

The |NSC| of wavelength (λ) exhibits a non-monotonic trend. In the shortwave band, the higher |NSC| indicates that MAC is more sensitive to changes in λ, reflecting the significant absorption of BC in this range. In the longwave band, |NSC| remains slightly above unity, suggesting that the sensitivity of MAC to λ decreases, which is also due to the inherently weaker absorption of BC at longer wavelengths.

The Sobol variance decomposition shown in Figure 6(b) is performed on the simulated MAC at a wavelength of 550 nm. Wavelength λ ranks first with a variance contribution of 61.9%, making it the dominant factor governing variations in MAC, consistent with the high |NSC| identified in the shortwave band in the NSC analysis. D_p/D_{BC} ranks second with a contribution of 33.19%, in agreement with the conclusion of high sensitivity of this parameter in the shell-thickening region drawn from the NSC analysis. Moreover, the total-order indices of D_{BC} far exceed the corresponding first-order indices, indicating that its influence on MAC is dominated by nonlinear interactions with other parameters rather than by its individual effects.

It should be noted that although Im and λ contribute the most to the total variance, they are prescribed external inputs for optical calculations. In contrast, the parameter D_p/D_{BC}, as the second-largest contributing factor, describes the internal mixing structure within BC particles. However, under the default CAM6 configuration, it exhibits objectively significant deviations from multiple field observations. Therefore, D_p/D_{BC} has been identified as the primary target for observational constraints and is the most effective control variable for improving the simulation of BC optical properties. Based on these findings, this study developed the D_{BC}-constrained scheme and the f_{BC}-constraint scheme. The essence of these two observation-constrained schemes is to address the issue of excessive BC coating by introducing particles that do not contain BC.

3.2 D_{BC}-constrained Scheme

BC core size is a first-order control on absorption, yet in modal schemes it is not an independent property of the emitted aerosol but a consequence of how BC mass is distributed among the modes. Figure 7 compares the simulated distributions of the

https://doi.org/10.5194/egusphere-2026-6748
Preprint. Discussion started: 19 November 2026
© Author(s) 2026. CC BY 4.0 License.

D_{BC} (solid bars) and the D_p (hatched bars) in the primary carbon mode (red) and the accumulation mode (blue) of CAM6, with the observed freshly emitted BC from FF and BB sources (Bond et al., 2013). In the current framework, the simulated D_{BC} are systematically underestimated because BC mass is spread evenly over each mode. To reduce the structural bias in BC core size, we prescribe D_{BC} from observations of FF (red dashed line) and BB (blue dashed line) emissions as the model constraints. In CAM6, both BC emission sources feed the primary carbon and accumulation modes simultaneously during BC mixing, except that BB-derived particles are larger and enter the accumulation mode directly. Note that the observed number median diameters of FF and BB are 70 nm and 140 nm, with geometric standard deviations of 1.7 and 1.4, respectively, and volume equivalent diameters are shown in figure 7.

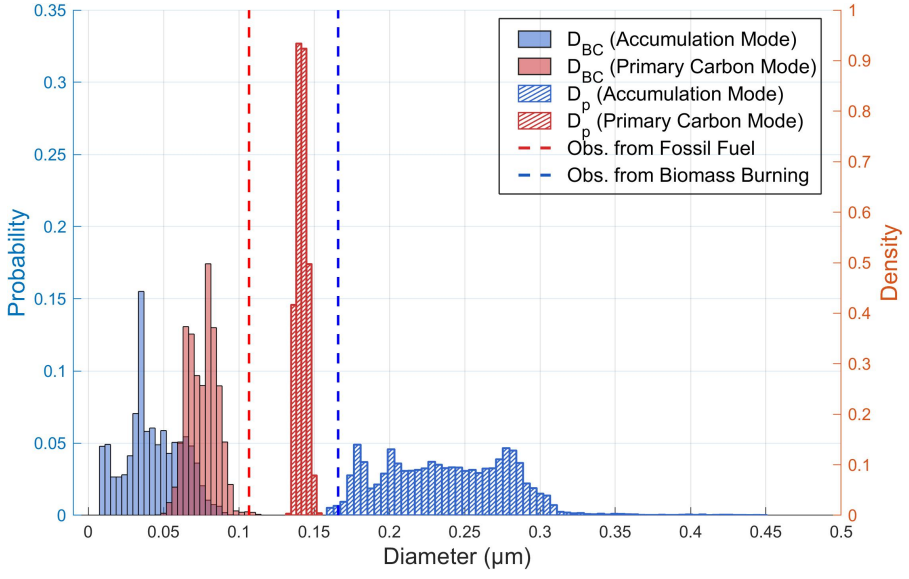


Figure 7. Size distributions of the BC core diameter (D_{BC}, solid bars) and total particle diameter (D_p, hatched bars) for the accumulation mode (blue) and primary carbon mode (red) simulated by CAM6, compared with observations of freshly emitted BC size from fossil-fuel (FF, red dashed lines) and biomass-burning (BB, blue dashed lines) sources reported by Bond et al. (2013).

Figure 8 compares the distributions of the size ratio D_p/D_{BC} for fresh and aged BC between the default scheme and D_{BC}-constrained scheme, and evaluates the regional performance against in-situ observations over the six high-concentration regions. The default scheme produces broad D_p/D_{BC} distributions, in particular for the

https://doi.org/10.5194/egusphere-2026-6748
Preprint. Discussion started: 19 November 2026
© Author(s) 2026. CC BY 4.0 License.

accumulation mode, reflecting an excessively thick simulated coating. The D_{BC}-constrained scheme substantially narrows the distribution range. In the regional comparison, the default scheme universally overestimates D_p/D_{BC} relative to the in-situ observations, whereas the new scheme suppresses this deviation and removes the extreme high values (Yoo et al., 2025; Kompalli et al., 2020; Taylor et al., 2020; Holanda et al., 2023; Sharma et al., 2017; Zanatta et al., 2018). Notably, the magnitude of the correction exhibits pronounced spatial heterogeneity. The correction is most pronounced in South Asia and North/South America. In particular, the values are closer to the observations in the accumulation mode constrained by VED_{BB}.

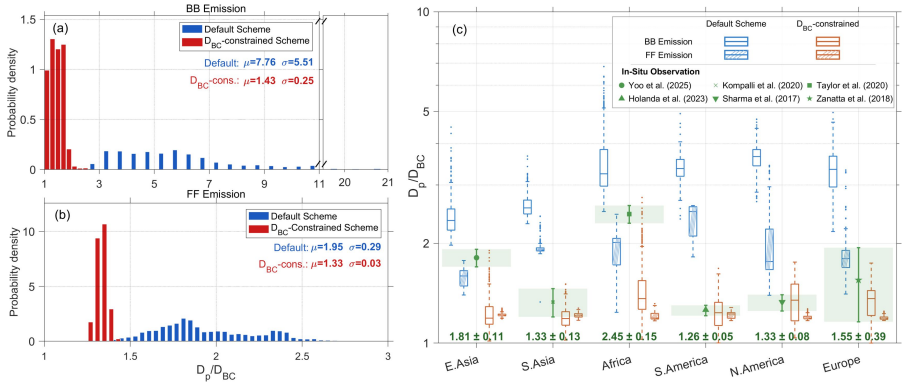


Figure 8. Probability density distributions of the particle-to-BC core diameter ratio (D_p/D_{BC}) for the default (blue) and D_{BC}-constrained (red) schemes: **(a)** Accumulation mode constrained by VED_{BB} with a bin width of 0.5 and 0.2 for default scheme and D_{BC}-constrained scheme respectively; **(b)** Primary carbon mode constrained by VED_{FF} with a bin width of 0.04. **(c)** Regional box-and-whisker comparison of simulated D_p/D_{BC} against in-situ observations across six major source regions (East Asia, South Asia, Africa, South America, North America, Europe). Hollow and hatched boxes denote accumulation and primary mode populations, respectively. Green markers with error bars show field observations, with detailed ranges reported below each region.

To evaluate the optical simulation performance of the D_{BC}-constrained scheme, 1−SSA at 440 nm is compared with AERONET observations from 2010 to 2020 over the six source regions, that is, North America, Europe, East Asia, South America, Africa and South Asia (Figure 9). Globally, the default scheme overestimates 1−SSA by 36%, whereas the D_{BC}-constrained scheme reproduces the observed distribution

https://doi.org/10.5194/egusphere-2026-6748
Preprint. Discussion started: 19 November 2026
© Author(s) 2026. CC BY 4.0 License.

closely, reducing the |NMB| to 3%. Regionally, |NMB| of the modeled mean values are reduced by 67.3%, 37.8%, 70.6%, 46.5%, 15.9% and 46.4% over the six high-concentration regions above, respectively. The improvement over Africa is comparatively limited and the RMSE reduction is modest (~20%). The regional contrast in performance is consistent with the corresponding changes in D_p/D_{BC} (Figure 8). This confirms that accurate representation of BC microphysical properties is an important pathway toward improved simulations of BC optical properties.

Under the default model configuration, the simulated D_p/D_{BC} spans a wide range of 1.5-15, as illustrated in Figure 8. Within this range, |NSC| exhibits oscillatory and amplified growth with increasing the ratio size, indicating that minor biases in D_p/D_{BC} can be nonlinearly magnified in the simulated MAC. In contrast, the D_{BC}-constrained scheme tightly compresses the D_p/D_{BC} distribution within a physically reasonable range of 1-2. In this optimized regime, |NSC| remains consistently close to unity and varies smoothly without the pronounced oscillatory peaks observed in the default simulation (Figure 10). This notable reduction in parameter sensitivity demonstrates that the constrained BC core diameter greatly weakens the dependence of MAC on D_p/D_{BC} variability, thereby substantially improving the numerical stability and physical robustness of BC optical simulations.

In summary, the D_{BC}-constrained scheme only imposes physical constraints on the BC particle size. It not only corrects the systematic biases of the default scheme, achieving 16%-70% improvements in absorption simulation across various regions, but also ensures stable optical outputs when microphysical inputs are uncertain. This is of great significance for reducing the uncertainty in BC direct radiative forcing estimates in climate models.

https://doi.org/10.5194/egusphere-2026-6748
Preprint. Discussion started: 19 November 2026
© Author(s) 2026. CC BY 4.0 License.

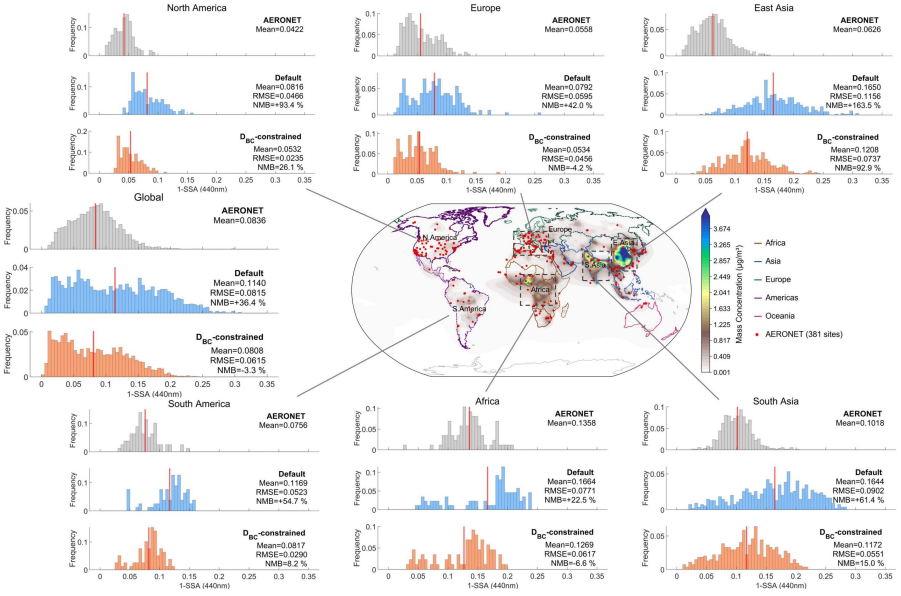


Figure 9. Comparison of simulated 1−SSA at 440 nm among the default, D_{BC}-constrained schemes of CAM6 and AERONET observations. Regional comparisons are presented for North America, Europe, East Asia, South America, Africa, and South Asia, with the global comparison. The central panel shows the global distribution of BC mass concentration, with AERONET sites used for the evaluation (red dots). Mean values of 1−SSA are represented by red lines in histograms. The monthly AERONET data are from 2010 to 2020.

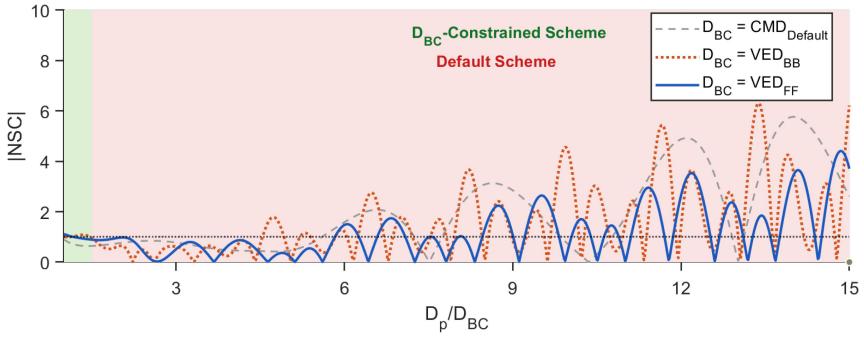


Figure 10. Normalized sensitivity coefficient |NSC| of BC absorption at 440 nm to the particle-to-core diameter ratio (D_p/D_{BC}), evaluated for a coated BC particle under three core-size settings, including the default-scheme modal core diameter ($CMD_{Default}$; gray dashed), VED_{BB} (orange dotted), and VED_{FF} (blue solid). The horizontal dotted

https://doi.org/10.5194/egusphere-2026-6748
Preprint. Discussion started: 19 November 2026
© Author(s) 2026. CC BY 4.0 License.

line marks |NSC| = 1. Shaded areas indicate the typical D_p/D_{BC} ranges of the D_{BC}-constrained scheme (green; $D_p/D_{BC} \leq 2$) and the default scheme (red; $D_p/D_{BC} \leq 15$).

3.3 f_{BC}-constrained Scheme

In contrast to the globally uniform D_{BC} constraint, the number fraction of BC-containing particles f_{BC} exhibits strong regional variability, which reflects spatial differences in emission density and aerosol aging. This feature therefore warrants regionally specified observational constraints, as implemented in the f_{BC}-constrained scheme. Figure 11a reveals the MAC responses of the default and f_{BC}-constrained schemes across different aerosol modes as a function of the coating thickness (D_p/D_{BC}), as well as the overall MAC behavior. The MAC values of the accumulation mode are consistently higher than those of the primary carbon mode. In the thin-coating regime, MAC exhibits low sensitivity to D_p/D_{BC}, and the discrepancies between the two schemes are limited. As the coating thickness increases further, MAC rises nonlinearly and rapidly, with notably higher MAC simulated by the new f_{BC}-constrained scheme relative to the default scheme, and this improvement is most prominent in the accumulation mode.

Figure 11b compares MAC across representative regions, including Beijing, Nanjing, Guangzhou, Africa, Chengdu, and Ascension Island. These locations are selected to represent different BC emission sources and atmospheric backgrounds. Beijing, Nanjing, Guangzhou and Chengdu are located in China's major urban agglomerations, namely the Beijing-Tianjin-Hebei Urban Agglomeration (BTH), Yangtze River Delta Urban Agglomeration (YRD), Pearl River Delta Urban Agglomeration (PRD) and Chengdu-Chongqing Urban Agglomeration (CC), all of which are characterized by dense fossil fuel (FF) emissions. Africa is a major source region for biomass burning (BB) globally, and Ascension Island, located in the central South Atlantic, receives transoceanic transport of BC plumes from Africa, making it a classic site for studying aged BC under long-range transport conditions. The inclusion of these observational sites provides comprehensive validation of the f_{BC}-constrained scheme's applicability under two typical emission sources.

The results show that the f_{BC}-constraint scheme effectively reduces the |NMB| values of simulated MAC in five of the six selected regions. The improvement is largest over Beijing (68%), followed by Guangzhou (60%), Africa (58%), Nanjing

https://doi.org/10.5194/egusphere-2026-6748
Preprint. Discussion started: 19 November 2026
© Author(s) 2026. CC BY 4.0 License.

(28%), and Ascension Island (13%). In the Chengdu region, the |NMB| variation in the simulation results is only about 1%, which falls within the range of observational uncertainty. However, the f_{BC} used for the Chengdu simulation was derived from observations at the Emei Mountain site. This station is located on the western edge of the Sichuan Basin and serves as a high-altitude background station, whereas the MAC observational data were collected in the urban area of Chengdu. Differences in spatial representativeness between the two locations may introduce errors in the comparative evaluation. Additionally, the mixing states of BC exhibit significant seasonal variations with the complex aerosol aging environment in the Sichuan Basin. Consequently, a single fixed f_{BC} value is insufficient to fully characterize the local distribution of BC. The above results indicate that the f_{BC}-constraint scheme enables local optimization based on regional f_{BC} observational data, but lacks a universal correction capability.

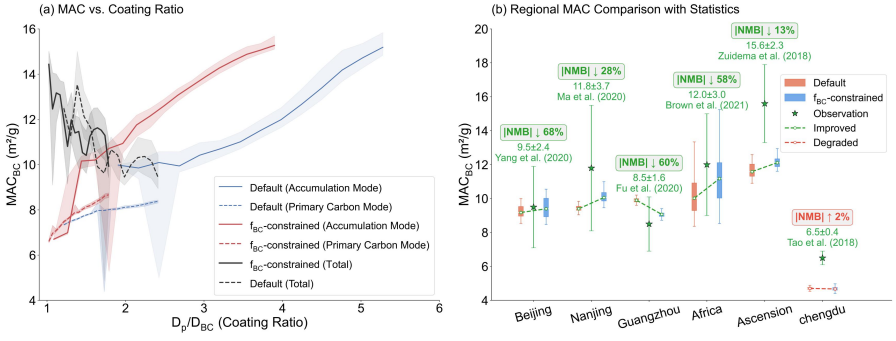


Figure 11. Evaluation of the f_{BC}-constrained scheme on MAC of BC. **(a)** MAC of BC as a function of D_p/D_{BC} for the accumulation mode, primary carbon mode, and their combined total. Solid and dashed lines represent the median MAC of the f_{BC}-constrained scheme and the default scheme, respectively. Shaded bands denote the interquartile range of MAC within each D_p/D_{BC} bin, reflecting spatial-temporal variability across studied regions and months. **(b)** Regional comparison of simulated MAC against observations at Beijing, Nanjing, Guangzhou, Africa, Chengdu, and Ascension Island. Green (red) dashed lines indicate the decline (increase) of the |NMB| relative to the default scheme. Star markers with error bars represent observed MAC.

The D_{BC}-constrained scheme addresses the issue of excessive coating in global models, while the f_{BC}-constrained scheme further considers the regional heterogeneity

https://doi.org/10.5194/egusphere-2026-6748
Preprint. Discussion started: 19 November 2026
© Author(s) 2026. CC BY 4.0 License.

of BC distribution, enabling targeted MAC corrections in observation-constrained regions. However, the applicability of the f_{BC}-constrained scheme is limited by the availability of regional f_{BC} observations, making it less universal than the D_{BC}-constrained scheme. Moreover, in regions with high f_{BC} variability, fixing a single f_{BC} value yields limited improvement. Therefore, the f_{BC}-constrained scheme is better suited as a local supplement to the D_{BC}-constrained framework, rather than serving as an independent global scheme alternative.

4. Conclusions

In this study, we conduct single-particle sensitivity experiments and reveal pronounced and size-dependent optical responses to BC mixing-state assumptions. The VM treatment dilutes BC absorption via volume-averaged refractive indices and produces lower MAC than the CS model under thick-coating conditions. Sobol variance decomposition identifies wavelength as the largest contributor to MAC variance, while the size ratio D_p/D_{BC} ranks second and represents the dominant controllable microphysical parameter. Under default CAM6 configuration limits, |NSC| of MAC increases in an oscillatory and amplifying manner with rising D_p/D_{BC}, such that microphysical biases propagate into substantial optical errors. These findings establish the size ratio D_p/D_{BC} as the primary target for observational constraints. Two observation-constrained BC optical schemes were subsequently proposed within the CAM6-MAM4 framework, namely the D_{BC}-constrained scheme and the f_{BC}-constrained scheme.

The D_{BC}-constrained scheme substitutes volume-derived core diameters with observationally constrained values, assigning VED_{FF} to the primary carbon mode and VED_{BB} to the accumulation mode. The global mean D_p/D_{BC} decreases from 6.3 to 2.1, and the physically implausible high-value tail is eliminated, yielding coating statistics consistent with SP2 field observations. Against AERONET observation, this scheme reduces global |NMB| of 1−SSA from 36% to 3%, with regional |NMB| reduced by 16%-70%. As shown by NSC curves, constraining D_p/D_{BC} within physically reasonable bounds greatly improves the numerical stability of optical calculations under microphysical uncertainties. The f_{BC}-constrained scheme further incorporates spatially variable number fraction derived from in situ observations. Regional comparisons against in-situ MAC observation yield |NMB| reductions of 13%-68% in five of the six target regions. Limited by regional observational availability, the

https://doi.org/10.5194/egusphere-2026-6748
Preprint. Discussion started: 19 November 2026
© Author(s) 2026. CC BY 4.0 License.

f_{BC}-constrained scheme serves best as a local complement to the globally applicable D_{BC}-constrained framework rather than a standalone alternative.

Both schemes provide computationally-efficient and practical pathways to improve the accuracy of BC optical simulations. Targeted constraints on the leading sensitive parameter D_p/D_{BC} simultaneously correct systematic absorption biases and dampen error amplification driven by microphysical uncertainties, which is of direct relevance to narrowing the uncertainty range of BC direct radiative forcing estimates in climate models.

Code availability

The CESM version 2 source codes in this study are available at https://doi.org/10.5281/zenodo.23827271 (Chen, 2026b).

Data availability

The observational data of aerosol SSA from ground-based sun-photometer sites AERONET, can be accessed at https://doi.org/10.5281/zenodo.23827220 (Chen, 2026a).

Author contributions

NC and GC designed the research, processed and analyzed observational and model data. WA conceived the idea of this work and contributed to acquiring funding. All co-authors wrote the manuscript and revised the manuscript.

Acknowledgements

NC and GC contributed equally to this work and should be considered as co-first authors. The authors thank CESM-CAM developers for making their code publicly available.

Financial support

This research has been supported by the Foundation for Innovative Research Groups of the National Natural Science Foundation of China (grant no. 42275070).

https://doi.org/10.5194/egusphere-2026-6748
Preprint. Discussion started: 19 November 2026
© Author(s) 2026. CC BY 4.0 License.

Competing interests

The contact author has declared that none of the authors has any competing interests.

References

Archer, G. E. B., Saltelli, A., and Sobol, I. M.: Sensitivity measures, ANOVA-like techniques and the use of bootstrap, J. Stat. Comput. Simul., 58, 99–120, https://doi.org/10.1080/00949659708811825, 1997.

Bond, T. C. and Bergstrom, R. W.: Light absorption by carbonaceous particles: An investigative review, Aerosol Sci. Technol., 40, 27–67, https://doi.org/10.1080/02786820500421521, 2006.

Bond, T. C., Doherty, S. J., Fahey, D. W., Forster, P. M., Berntsen, T., DeAngelo, B. J., Flanner, M. G., Ghan, S., Kärcher, B., Koch, D., Kinne, S., Kondo, Y., Quinn, P. K., Sarofim, M. C., Schultz, M. G., Schulz, M., Venkataraman, C., Zhang, H., Zhang, S., Bellouin, N., Guttikunda, S. K., Hopke, P. K., Jacobson, M. Z., Kaiser, J. W., Klimont, Z., Lohmann, U., Schwarz, J. P., Shindell, D., Storelvmo, T., Warren, S. G., and Zender, C. S.: Bounding the role of black carbon in the climate system: A scientific assessment, J. Geophys. Res.-Atmos., 118, 5380–5552, https://doi.org/10.1002/jgrd.50171, 2013.

Brown, H., Liu, X., Pokhrel, R., Murphy, S., Lu, Z., Saleh, R., Mielonen, T., Kokkola, H., Bergman, T., Myhre, G., Skeie, R. B., Watson-Paris, D., Stier, P., Johnson, B., Bellouin, N., Schulz, M., Vakkari, V., Beukes, J. P., van Zyl, P. G., Liu, S., and Chand, D.: Biomass burning aerosols in most climate models are too absorbing, Nat. Commun., 12, 277, https://doi.org/10.1038/s41467-020-20482-9, 2021.

Cappa, C. D., Onasch, T. B., Massoli, P., Worsnop, D. R., Bates, T. S., Cross, E. S., Davidovits, P., Hakala, J., Hayden, K. L., Jobson, B. T., Kolesar, K. R., Lack, D. A., Lerner, B. M., Li, S.-M., Mellon, D., Nuaaman, I., Olfert, J. S., Petäjä, T., Quinn, P. K., Chen, S.: Radiative Absorption Enhancements Due to the Mixing State of Atmospheric Black Carbon. Science, 337(6098): 1078-1081, https://doi.org/10.1126/science.1223447, 2012.

Chen, G.: AERONET data, Zenodo [dataset], https://doi.org/10.5281/zenodo.23827220, 2026a.

Chen, G.: Source codes of CESM, Zenodo [code], https://doi.org/10.5281/zenodo.23827271, 2026b.

Chen, G., Wang, J., Wang, Y., Wang, J., Jin, Y., Cheng, Y., Yin, Y., Liao, H., Ding, A., Wang, S., Hao, J., and Liu, C.: An aerosol optical module with observation-constrained black

https://doi.org/10.5194/egusphere-2026-6748
Preprint. Discussion started: 19 November 2026
© Author(s) 2026. CC BY 4.0 License.



carbon properties for global climate models, J. Adv. Model. Earth Syst., 15, e2022MS003501, https://doi.org/10.1029/2022MS003501, 2023.

Chen, G., Liu, C., Wang, J., Yin, Y., and Wang, Y.: Accounting for black carbon mixing state, nonsphericity, and heterogeneity effects in its optical property parameterization in a climate model, J. Geophys. Res.-Atmos., 129, e2024JD041135, https://doi.org/10.1029/2024JD041135, 2024.

Chen, L., Zhang, F., Yan, P., Wang, X., Sun, L., Li, Y., Zhang, X., Sun, Y., and Li, Z.: The large proportion of black carbon (BC)-containing aerosols in the urban atmosphere, Environ. Pollut., 263, 114507, https://doi.org/10.1016/j.envpol.2020.114507, 2020.

Cheung, H. H. Y., Tan, H., Xu, H., Li, F., Wu, C., Yu, J. Z., and Chan, C. K.: Measurements of non-volatile aerosols with a VTDMA and their correlations with carbonaceous aerosols in Guangzhou, China, Atmos. Chem. Phys., 16, 8431–8446, https://doi.org/10.5194/acp-16-8431-2016, 2016.

Curci, G., Alyuz, U., Barò, R., Bianconi, R., Bieser, J., Christensen, J. H., Colette, A., Farrow, A., Francis, X., Jiménez-Guerrero, P., Im, U., Liu, P., Manders, A., Palacios-Peña, L., Prank, M., Pozzoli, L., Sokhi, R., Solazzo, E., Tuccella, P., Unal, A., Vivanco, M. G., Hogrefe, C., and Galmarini, S.: Modelling black carbon absorption of solar radiation: combining external and internal mixing assumptions, Atmos. Chem. Phys., 19, 181–204, https://doi.org/10.5194/acp-19-181-2019, 2019.

Danabasoglu, G., Lamarque, J.-F., Bacmeister, J., Bailey, D. A., DuVivier, A. K., Edwards, J., Emmons, L. K., Fasullo, J., Garcia, R., Gettelman, A., Hannay, C., Holland, M. M., Large, W. G., Lauritzen, P. H., Lawrence, D. M., Lenaerts, J. T. M., Lindsay, K., Lipscomb, W. H., Mills, M. J., Neale, R., Oleson, K. W., Otto-Bliesner, B., Phillips, A. S., Sacks, W., Tilmes, S., van Kampenhout, L., Vertenstein, M., Bertini, A., Dennis, J., Deser, C., Fischer, C., Fox-Kemper, B., Kay, J. E., Kinnison, D., Kushner, P. J., Larson, V. E., Long, M. C., Mickelson, S., Moore, J. K., Nienhouse, E., Polvani, L., Rasch, P. J., and Strand, W. G.: The Community Earth System Model version 2 (CESM2), J. Adv. Model. Earth Syst., 12, e2019MS001916, https://doi.org/10.1029/2019MS001916, 2020.

Denjean, C., Brito, J., Libois, Q., Mallet, M., Bourrianne, T., Burnet, F., Dupuy, R., Flamant, C., and Knippertz, P.: Unexpected biomass burning aerosol absorption enhancement explained by black carbon mixing state, Geophys. Res. Lett., 47, e2020GL089055, https://doi.org/10.1029/2020GL089055, 2020.

Ditas, J., Ma, N., Zhang, Y., Assmann, D., Neumaier, M., Riede, H., Karu, E., Williams, J., Scharffe, D., Wang, Q., Saturno, J., Schwarz, J. P., Katich, J. M., McMeeking, G. R., Zahn, A., Hermann, M., Brenninkmeijer, C. A. M., Andreae, M. O., Pöschl, U., Su, H., and Cheng, Y.: Strong impact of wildfires on the abundance and aging of black carbon in the lowermost stratosphere, Proc. Natl. Acad. Sci. USA, 115, E11595–E11603,

https://doi.org/10.5194/egusphere-2026-6748
Preprint. Discussion started: 19 November 2026
© Author(s) 2026. CC BY 4.0 License.

https://doi.org/10.1073/pnas.1806868115, 2018.

Dobracki, A., Lewis, E. R., Sedlacek III, A. J., Tatro, T., Zawadowicz, M. A., and Zuidema, P.: Burning conditions and transportation pathways determine biomass-burning aerosol properties in the Ascension Island marine boundary layer, Atmos. Chem. Phys., 25, 2333–2363, https://doi.org/10.5194/acp-25-2333-2025, 2025.

Dubovik, O. and King, M. D.: A flexible inversion algorithm for retrieval of aerosol optical properties from Sun and sky radiance measurements, J. Geophys. Res. Atmos., 105, 20673–20696, https://doi.org/10.1029/2000JD900282, 2000.

Everett, J. T., Newton, E. N., and Odum, M. M.: A review of progress in constraining global black carbon climate effects, Earth Syst. Environ., 6, 771–785, https://doi.org/10.1007/S41748-022-00313-1, 2022.

Fierce, L., Riemer, N., and Bond, T. C.: Explaining variance in black carbon's aging timescale, Atmos. Chem. Phys., 15, 3173–3191, https://doi.org/10.5194/acp-15-3173-2015, 2015.

Fierce, L., Onasch, T. B., Cappa, C. D., Mazzoleni, C., China, S., Bhandari, J., Davidovits, P., Fischer, D. A., Helgestad, T., Lambe, A. T., Sedlacek III, A. J., Smith, G. D., and Wolff, L.: Radiative absorption enhancements by black carbon controlled by particle-to-particle heterogeneity in composition, Proc. Natl. Acad. Sci. USA, 117, 5196–5203, https://doi.org/10.1073/pnas.1919723117, 2020.

Fu, Y., Peng, X., Guo, Z., Peng, L., Lin, Q., Li, L., Li, M., Chen, D., Zhang, G., Bi, X., Wang, X., and Sheng, G.: Filter-based absorption enhancement measurement for internally mixed black carbon particles over southern China, Sci. Total Environ., 762, 144194, https://doi.org/10.1016/j.scitotenv.2020.144194, 2021.

Ghan, S. J. and Zaveri, R. A.: Parameterization of optical properties for hydrated internally mixed aerosol, J. Geophys. Res. Atmos., 112, D10201, https://doi.org/10.1029/2006JD007927, 2007.

Hess, M., Koepke, P., and Schult, I.: Optical properties of aerosols and clouds: the software package OPAC, Bull. Am. Meteorol. Soc., 79, 831–844, https://doi.org/10.1175/1520-0477(1998)079<0831:OPOAAC>2.0.CO;2 , 1998.

Holanda, B. A., Pöhlker, M. L., Walter, D., Saturno, J., Sörgel, M., Ditas, J., Ditas, F., Schulz, C., Franco, M. A., Wang, Q., Donth, T., Artaxo, P., Barbosa, H. M. J., Borrmann, S., Braga, R., Brito, J., Cheng, Y., Dollner, M., Kaiser, J. W., Klimach, T., Knote, C., Krüger, O. O., Fütterer, D., Lavrič, J. V., Ma, N., Machado, L. A. T., Ming, J., Morais, F. G., Paulsen, H., Sauer, D., Schlager, H., Schneider, J., Su, H., Weinzierl, B., Walser, A., Wendisch, M., Ziereis, H., Zöger, M., Pöschl, U., Andreae, M. O., and Pöhlker, C.: Influx of African biomass burning aerosol during the Amazonian dry season through layered transatlantic transport of black carbon-rich smoke, Atmos. Chem. Phys., 20, 4757–4785, https://doi.org/10.5194/acp-20-4757-2020, 2020.

https://doi.org/10.5194/egusphere-2026-6748
Preprint. Discussion started: 19 November 2026
© Author(s) 2026. CC BY 4.0 License.



785 Holanda, B. A., Franco, M. A., Walter, D., Artaxo, P., Carbone, S., Cheng, Y., Chowdhury, S.,
786 Ditas, F., Gysel-Beer, M., Klimach, T., Kremper, L. A., Krüger, O. O., Lavric, J. V.,
787 Lelieveld, J., Ma, C., Machado, L. A. T., Modini, R. L., Morais, F. G., Pozzer, A.,
788 Saturno, J., Su, H., Wendisch, M., Wolff, S., Pöhlker, M. L., Andreae, M. O., Pöschl, U.,
789 and Pöhlker, C.: African biomass burning affects aerosol cycling over the Amazon,
790 Commun. Earth Environ., 4, 154, https://doi.org/10.1038/s43247-023-00795-5, 2023.
791 Holben, B. N., Eck, T. F., Slutsker, I., Tanré, D., Buis, J. P., Setzer, A., Vermote, E., Reagan, J.
792 A., Kaufman, Y. J., Nakajima, T., Lavenu, F., Jankowiak, I., and Smirnov, A.: AERONET
793 – A federated instrument network and data archive for aerosol characterization, Remote
794 Sens. Environ., 66, 1–16, https://doi.org/10.1016/S0034-4257(98)00031-5, 1998.
795 Iacono, M. J., Delamere, J. S., Mlawer, E. J., Shephard, M. W., Clough, S. A., and Collins, W.
796 D.: Radiative forcing by long-lived greenhouse gases: Calculations with the AER
797 radiative transfer models, J. Geophys. Res.-Atmos., 113, D13103,
798 https://doi.org/10.1029/2008JD009944, 2008.
799 Jacobson, M. Z.: Strong radiative heating due to the mixing state of black carbon in
800 atmospheric aerosols, Nature, 409, 695–697, https://doi.org/10.1038/35055518, 2001.
801 Kodros, J. K., Hanna, S. J., Bertram, A. K., Leaitch, W. R., Schulz, H., Herber, A. B., Zanatta,
802 M., Burkart, J., Willis, M. D., Abbatt, J. P. D., & Pierce, J. R.: Size-resolved mixing state
803 of black carbon in the Canadian high Arctic and implications for simulated direct
804 radiative effect, Atmos. Chem. Phys., 18, 11345–11361,
805 https://doi.org/10.5194/acp-18-11345-2018, 2018.
806 Kompalli, S. K., Suresh Babu, S. N., Satheesh, S. K., Krishna Moorthy, K., Das, T., Boopathy,
807 R., Liu, D., Darbyshire, E., Allan, J. D., Brooks, J., Flynn, M. J., and Coe, H.: Seasonal
808 contrast in size distributions and mixing state of black carbon and its association with
809 PM1.0 chemical composition from the eastern coast of India, Atmos. Chem. Phys., 20,
810 3965–3985, https://doi.org/10.5194/acp-20-3965-2020, 2020.
811 Li, F., Luo, B., Zhai, M., Liu, L., Zhao, G., Xu, H., Deng, T., Deng, X., Tan, H., Kuang, Y.,
812 and Zhao, J.: Black carbon content of traffic emissions significantly impacts black
813 carbon mass size distributions and mixing states, Atmos. Chem. Phys., 23, 6545–6558,
814 https://doi.org/10.5194/acp-23-6545-2023, 2023.
815 Liu, X., Easter, R. C., Ghan, S. J., Zaveri, R., Rasch, P., Shi, X., Lamarque, J.-F., Gettelman,
816 A., Morrison, H., Vitt, F., Conley, A., Park, S., Neale, R., Hannay, C., Ekman, A. M. L.,
817 Hess, P., Mahowald, N., Collins, W., Iacono, M. J., Bretherton, C. S., Flanner, M. G., and
818 Mitchell, D.: Toward a minimal representation of aerosols in climate models: description
819 and evaluation in the Community Atmosphere Model CAM5, Geosci. Model Dev., 5,
820 709–739, https://doi.org/10.5194/gmd-5-709-2012, 2012.
821 Liu, X., Ma, P.-L., Wang, H., Tilmes, S., Singh, B., Easter, R. C., Ghan, S. J., and Rasch, P. J.:

https://doi.org/10.5194/egusphere-2026-6748
Preprint. Discussion started: 19 November 2026
© Author(s) 2026. CC BY 4.0 License.

Description and evaluation of a new four-mode version of the Modal Aerosol Module (MAM4) within version 5.3 of the Community Atmosphere Model, Geosci. Model Dev., 9, 505–522, https://doi.org/10.5194/gmd-9-505-2016, 2016.

Ma, Y., Huang, C., Jabbour, H., Zheng, Z., Wang, Y., Jiang, Y., Zhu, W., Ge, X., Collier, S., and Zheng, J.: Mixing state and light absorption enhancement of black carbon aerosols in summertime Nanjing, China, Atmos. Environ., 222, 117141, https://doi.org/10.1016/j.atmosenv.2019.117141, 2020.

Romshoo, B., Müller, T., Pfeifer, S., Saturno, J., Nowak, A., Ciupek, K., Quincey, P., and Wiedensohler, A.: Optical properties of coated black carbon aggregates: numerical simulations, radiative forcing estimates, and size-resolved parameterization scheme, Atmos. Chem. Phys., 21, 12989–13010, https://doi.org/10.5194/acp-21-12989-2021, 2021.

Saltelli, A., Annoni, P., Azzini, I., Campolongo, F., Ratto, M., and Tarantola, S.: Variance based sensitivity analysis of model output. Design and estimator for the total sensitivity index, Comput. Phys. Commun., 181, 259–270, https://doi.org/10.1016/j.cpc.2009.09.018, 2010.

Schwarz, J. P., Gao, R. S., Fahey, D. W., Thomson, D. S., Watts, L. A., Wilson, J. C., Reeves, J. M., Darbeheshti, M., Baumgardner, D. G., Kok, G. L., Chung, S. H., Schulz, M., Hendricks, J., Lauer, A., Kärcher, B., Slowik, J. G., Rosenlof, K. H., Thompson, T. L., and Loewenstein, M.: Single-particle measurements of midlatitude black carbon and light-scattering aerosols from the boundary layer to the lower stratosphere, J. Geophys. Res.-Atmos., 111, D16207, https://doi.org/10.1029/2006JD007076, 2006.

Schwarz, J. P., Spackman, J. R., Fahey, D. W., Gao, R. S., Lohmann, U., Stier, P., Watts, L. A., Thomson, D. S., Lack, D. A., Pfister, L., Mahoney, M. J., Baumgardner, D., Wilson, J. C., and Reeves, J. M.: Coatings and their enhancement of black carbon light absorption in the tropical atmosphere, J. Geophys. Res.-Atmos., 113, D03203, https://doi.org/10.1029/2007JD009042, 2008.

Sharma, S., Leaitch, W. R., Huang, L., Veber, D., Kolonjari, F., Zhang, W., Hanna, S. J., Bertram, A. K., and Ogren, J. A.: An evaluation of three methods for measuring black carbon in Alert, Canada, Atmos. Chem. Phys., 17, 15225–15243, https://doi.org/10.5194/acp-17-15225-2017, 2017.

Shiraiwa, M., Kondo, Y., Moteki, N., Takegawa, N., Miyazaki, Y., and Blake, D. R.: Evolution of mixing state of black carbon in polluted air from Tokyo, Geophys. Res. Lett., 34, L16805, https://doi.org/10.1029/2007GL029819, 2007.

Sobol, I. M.: Global sensitivity indices for nonlinear mathematical models and their Monte Carlo estimates, Math. Comput. Simul., 55, 271–280, https://doi.org/10.1016/S0378-4754(00)00270-6, 2001.

https://doi.org/10.5194/egusphere-2026-6748
Preprint. Discussion started: 19 November 2026
© Author(s) 2026. CC BY 4.0 License.

Szopa, S., Naik, V., Adhikary, B., Artaxo, P., Berntsen, T., Collins, W. D., Fuzzi, S., Gallardo, L., Kiendler-Scharr, A., Klimont, Z., Liao, H., Unger, N., and Zanis, P.: Short-lived climate forcers, in: Climate Change 2021: The Physical Science Basis. Contribution of Working Group I to the Sixth Assessment Report of the Intergovernmental Panel on Climate Change, edited by: Masson-Delmotte, V., Zhai, P., Pirani, A., Connors, S. L., Péan, C., Berger, S., Caud, N., Chen, Y., Goldfarb, L., Gomis, M. I., Huang, M., Leitzell, K., Lonnoy, E., Matthews, J. B. R., Maycock, T. K., Waterfield, T., Yelekçi, O., Yu, R., and Zhou, B., Cambridge University Press, Cambridge, United Kingdom and New York, NY, USA, 817–921, https://doi.org/10.1017/9781009157896.008, 2021.

Tao, J., Zhang, Z., Wu, Y., Lin, Z., Cao, J., Shen, Z., and Zhang, R.: Characteristics of mass absorption efficiency of elemental carbon in urban Chengdu, Southwest China: implication for the coating effects on aerosol absorption, Aerosol Sci. Eng., 2, 33–41, https://doi.org/10.1007/s41810-018-0022-8, 2018.

Taylor, J. W., Wu, H., Szpek, K., Langridge, J. M., Williams, P. I., Flynn, M., Allan, J. D., Abel, S. J., Pitt, J., Cotterell, M. I., Fox, C., Davies, N. W., Haywood, J., and Coe, H.: Absorption closure in highly aged biomass burning smoke, Atmos. Chem. Phys., 20, 11201–11221, https://doi.org/10.5194/acp-20-11201-2020, 2020.

Toon, O. B. and Ackerman, T. P.: Algorithms for the calculation of scattering by stratified spheres, Appl. Opt., 20, 3657–3660, https://doi.org/10.1364/AO.20.003657, 1981.

Wang, Y., Li, W., Huang, J., Liu, L., Pang, Y., He, C., Liu, F., Liu, D., Bi, L., Zhang, X., and Shi, Z.: Nonlinear enhancement of radiative absorption by black carbon in response to particle mixing structure, Geophys. Res. Lett., 48, e2021GL096437, https://doi.org/10.1029/2021GL096437, 2021.

Yang, M., Howell, S. G., Zhuang, J., and Huebert, B. J.: Attribution of aerosol light absorption to black carbon, brown carbon, and dust in China – interpretations of atmospheric measurements during EAST-AIRE, Atmos. Chem. Phys., 9, 2035–2050, https://doi.org/10.5194/acp-9-2035-2009, 2009.

Yoo, M., Cho, J., Sung, M., Lee, S., Kim, M., Ramu, A. G., Chung, H., Choi, J., Lee, T., Park, J., and Lee, H.: Aircraft observations of black carbon over the Yellow Sea and Seoul Metropolitan Area: Vertical profiles and air mass origin influence, J. Environ. Sci, https://doi.org/10.1016/j.jes.2025.10.034, 2025.

Yuan, Q., Wang, Y., Chen, Y., Yue, S., Zhang, J., Zhang, Y., Xu, L., Hu, W., Liu, D., Fu, P., Gao, H., and Li, W.: Measurement report: New insights into the mixing structures of black carbon on the eastern Tibetan Plateau – soot redistribution and fractal dimension enhancement by liquid–liquid phase separation, Atmos. Chem. Phys., 23, 9385–9399, https://doi.org/10.5194/acp-23-9385-2023, 2023.

Zanatta, M., Laj, P., Gysel, M., Baltensperger, U., Vratolis, S., Eleftheriadis, K., Kondo, Y.,

https://doi.org/10.5194/egusphere-2026-6748
Preprint. Discussion started: 19 November 2026
© Author(s) 2026. CC BY 4.0 License.



Dubuisson, P., Winiarek, V., Kazadzis, S., Tunved, P., and Jacobi, H.-W.: Effects of mixing state on optical and radiative properties of black carbon in the European Arctic, Atmos. Chem. Phys., 18, 14037–14057, https://doi.org/10.5194/acp-18-14037-2018, 2018.

Zhao, X., Liu, X., Burrows, S. M., and Shi, Y.: Effects of marine organic aerosols as sources of immersion-mode ice-nucleating particles on high-latitude mixed-phase clouds, Atmos. Chem. Phys., 21, 2305–2327, https://doi.org/10.5194/acp-21-2305-2021, 2021.

Zuidema, P., Sedlacek III, A. J., Flynn, C., Springston, S., Delgadillo, R., Zhang, J., Aiken, A. C., Koontz, A., and Muradyan, P.: The Ascension Island boundary layer in the remote southeast Atlantic is often smoky, Geophys. Res. Lett., 45, 4456–4465, https://doi.org/10.1002/2017GL076926, 2018.